

Physics-informed neural network for material identification via distortion-robust polychromatic x-ray attenuation correction in photon-counting detectors

Xin Yan(闫欣), Jie Zhang(张杰), Kai He(何凯), Yiheng Liu(刘毅恒), Yuetong Zhao(赵悦彤), Gang Wang(王刚), Xinlong Chang(常新龙), and Youwei Zhang(张有为)

Citation: Chin. Phys. B, 2026, 35 (**5**): 050702. DOI: 10.1088/1674-1056/ae5a13
http://cpb.iphy.ac.cn; http://iopscience.iop.org/cpb

What follows is a list of articles you may be interested in

Improved physics-informed neural networks incorporating lattice Boltzmann method optimized by tanh robust weight initialization

Chenghui Yang(杨程晖), Minglei Shan(单鸣雷), Mengyu Feng(冯梦宇), Ling Kuai(蒯玲), Yu Yang(杨雨), Cheng Yin(殷澄), and Qingbang Han(韩庆邦)

Chin. Phys. B, 2025, 34 (**11**): 110701. DOI: 10.1088/1674-1056/adfc43

TCAS-PINN: Physics-informed neural networks with a novel temporal causality-based adaptive sampling method

Jia Guo(郭嘉), Haifeng Wang(王海峰), Shilin Gu(古仕林), and Chenping Hou(侯臣平)

Chin. Phys. B, 2024, 33 (**5**): 050701. DOI: 10.1088/1674-1056/ad21f3

Measurement of the relative neutron sensitivity curve of a $LaBr_3$(Ce) scintillator based on the CSNS Back-n white neutron source

Jian Liu(刘建), Dongming Wang(王东明), Yuecheng Fu(甫跃成), Zhongbao Li(李忠宝), Han Yi(易晗), and Longtao Yi(易龙涛)

Chin. Phys. B, 2023, 32 (**10**): 100703. DOI: 10.1088/1674-1056/acca08

ESR-PINNs: Physics-informed neural networks with expansion-shrinkage resampling selection strategies

Jianan Liu(刘佳楠), Qingzhi Hou(侯庆志), Jianguo Wei(魏建国), and Zewei Sun(孙泽玮)

Chin. Phys. B, 2023, 32 (**7**): 070702. DOI: 10.1088/1674-1056/acc1d5

X-ray focusing using an x-ray lens composed of multi-square polycapillary slices

Kai Pan(潘凯), Tian-Cheng Yi(易天成), Zhao Wang(王曌), Mo Zhou(周末), Yu-De Li(李玉德), Zhi-Guo Liu(刘志国), Xiao-Yan Lin(林晓燕), and Tian-Xi Sun(孙天希)

Chin. Phys. B, 2022, 31 (**2**): 020701. DOI: 10.1088/1674-1056/ac381a

---

Physics-informed neural network for material identification via distortion-robust polychromatic x-ray attenuation correction in photon-counting detectors

Xin Yan(闫欣)[1,2], Jie Zhang(张杰)[2,†], Kai He(何凯)[2,‡], Yiheng Liu(刘毅恒)[2], Yuetong Zhao(赵悦彤)[2], Gang Wang(王刚)[2], Xinlong Chang(常新龙)[1], and Youwei Zhang(张有为)[3]

[1] *Rocket Force University of Engineering, Xi'an* 710025, *China*

[2] *State Key Laboratory of Ultrafast Optical Science and Technology, Xi'an Institute of Optics and Precision Mechanics, Chinese Academy of Sciences, Xi'an* 710119, *China*

[3] *National Gravitation Laboratory, MOE Key Laboratory of Fundamental Physical Quantities Measurement, and School of Physics, Huazhong University of Science and Technology, Wuhan* 430074, *China*

(Received 12 February 2026; revised manuscript received 24 March 2026; accepted manuscript online 1 April 2026)

Spectral distortions in photon-counting detectors (PCDs) fundamentally limit the quantitative accuracy of material identification. While machine learning is used for compensation, current data-driven methods often lack physical constraints, limiting their interpretability and reliability across varying conditions. To address this issue, we propose a physics-informed neural network (PINN) framework that explicitly embeds the Beer–Lambert law into the learning architecture. By integrating an explicit differential layer to extract high-order curvature features from distorted spectra, the model enables direct inference of the effective atomic number and areal density. This approach effectively leverages the Z-dependent non-linear profile of the photoelectric effect, even when explicit absorption edges are outside the primary detection window. Simulation results establish a high-precision benchmark for Z_{eff} estimation in the target low-Z range (6–13), with an RMSE of 0.2111. Experimental validation on a CdZnTe-PCD further demonstrates that this accuracy improvement is preserved under realistic pulse pile-up and noise conditions, achieving an RMSE of 0.2457 and an R^2 of 0.9670. Compared with conventional physical correction methods (typically ± 0.5 error margin), the proposed framework provides improved precision, with 92.86% of Z_{eff} estimation errors falling within ± 0.4, corresponding to an approximately 20% tighter error bound. These results confirm that the proposed framework effectively mitigates spectral distortion, providing a robust, calibration-free solution for precise material identification of low-Z materials in industrial non-destructive testing.

Keywords: physics-informed neural networks (PINNs), photon-counting detectors (PCDs), material identification, x-ray imaging

PACS: 07.85.Fv, 07.05.Mh, 81.70.–q, 87.59.–e

DOI: 10.1088/1674-1056/ae5a13 **CSTR:** 32038.14.CPB.ae5a13

1. Introduction

Since Roentgen's seminal discovery in 1895, attenuation-based x-ray imaging has evolved into an indispensable tool for industrial non-destructive testing (NDT) and clinical diagnosis.[1–3] Based on the foundational dual-basis decomposition theory, modern imaging systems can quantitatively characterize material composition, a physical process detailed in classical radiological physics literature.[4,5] While conventional energy-integrating detectors (EIDs) are limited to intensity projections, photon-counting detectors (PCDs) represent a paradigm shift.[6] By resolving individual photon energies, PCDs theoretically enable high-contrast material identification and multi-energy decomposition.[7,8]

PCDs represent a paradigm shift in x-ray imaging. By resolving the energy of individual photons and recording pixel-wise spectral information, PCDs enable the retrieval of material-specific linear attenuation coefficients, $\mu(E)$, from a single polychromatic exposure. This capability theoretically facilitates direct material fingerprinting and quantitative decomposition. The linear attenuation coefficient $\mu(E)$ is an intrinsic physical property of a material uniquely determined by the atomic number Z and electron density ρ_{e}. For x-rays of energy E and incident flux $I_0(E)$ propagating through a material of thickness t, the transmitted intensity is governed by the Beer–Lambert law[5]

$$I(E) = I_0 \exp\left[-\mu(E)t\right]. \tag{1}$$

In practice, however, PCDs employing sensor materials like cadmium zinc telluride (CdZnTe) or silicon face significant challenges arising from the polychromatic nature of x-ray sources and complex detector response mechanisms, including pulse pile-up, fluorescence escape, charge sharing, and finite energy resolution.[9–15] Consequently, the measured projection spectrum deviates significantly from the true transmission spectrum.[16–18] The spectral distortion can be modeled

†Corresponding author. E-mail: zhangjie@opt.ac.cn

‡Corresponding author. E-mail: hekai@opt.ac.cn

© 2026 Chinese Physical Society and IOP Publishing Ltd. All rights, including for text and data mining, AI training, and similar technologies, are reserved.

via forward simulation, primarily accounting for: (1) the escape peak response, denoted as R_1, arising from characteristic fluorescence escape following photoelectric interactions; and (2) the response matrix R_2, characterizing spectral shifts toward lower energies due to charge sharing and peak broadening from finite energy resolution. Mathematically, the output spectrum results from a unidirectional transformation: the incident spectrum left-multiplied by the response matrix R_1R_2 (Fig. 1).

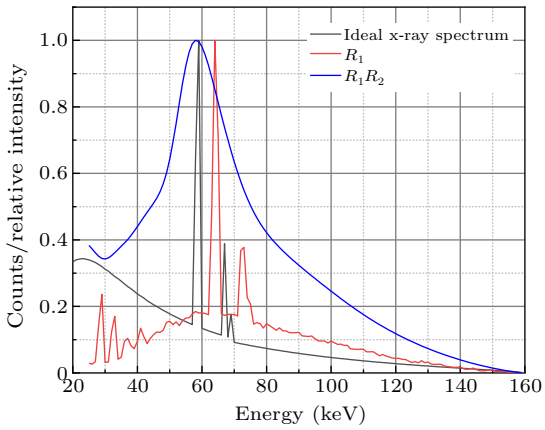


Fig. 1. Illustration of the x-ray spectral distortion mechanism in a PCD.

To mitigate spectral distortions, early research primarily focused on hardware optimizations and analytical corrections.[19,20] For instance, Hu *et al.*[21] proposed an FPGA-based pulse pile-up rejection technique, while Kimoto *et al.*[22,23] reported recent advances in detector electronics. Algorithmically, Shikhaliev[24] utilized K-edge filtering to enhance material separation, and Kimoto *et al.*[25] developed a polychromatic attenuation correction method for effective atomic number estimation. However, these methods often require complex calibration or specific hardware configurations.[26,27] Recently, deep learning has shown great potential in solving inverse imaging problems.[28–30] Data-driven strategies, such as convolutional neural networks (CNNs), have been applied to material decomposition in both medical CT and industrial NDT.[31–33] Despite progress in analytical correction and data-driven methods, significant challenges remain in PCD-based material identification. DRM-based inversion is inherently ill-posed, and deconvolution often amplifies measurement noise, causing numerical instability in material-parameter estimation. In contrast, purely data-driven deep learning methods avoid explicit inversion but often lack physical constraints from x-ray attenuation laws, limiting interpretability and reducing generalization under varying spectral distortion conditions.

To address these limitations, PINNs, originally introduced by Raissi *et al.*,[34] offer a new paradigm by embedding physical laws into the loss function. This approach has proven effective in various domains, from optical imaging[35] to electromagnetic optimization.[36] Recent studies in physics-guided inverse modeling have demonstrated the superiority of PINNs in solving complex inverse problems and governing partial differential equations.[37] To further enhance network convergence and training efficiency, advanced architectures incorporating adaptive sampling strategies have also been developed.[38] For example, Li *et al.*[39] successfully applied PINNs to low-temperature plasma parameter inversion, and Liu *et al.*[40] utilized them for nonlinear dynamics prediction. Moreover, Tian *et al.*[41] confirmed that incorporating prior physical information significantly improves model convergence and accuracy under small-sample conditions. However, to the best of our knowledge, there have been very limited reports on applying PINNs to material identification using PCDs, despite the strong need for physically constrained inversion under spectral distortion.

In this work, inspired by physics-guided inverse reconstruction strategies,[42] we propose a PINN framework for distortion-robust material identification in PCDs by explicitly embedding the Beer–Lambert law into end-to-end learning. The proposed architecture integrates an explicit differential feature extraction module to capture spectral slope and curvature information, which is closely related to the energy-dependent nonlinear behavior of the photoelectric effect. Based on the physical distinction between spectral shape and amplitude, we further design a decoupled inference scheme in which high-order differential features are used to estimate the effective atomic number, while intensity features are used to estimate areal density. By combining physics-constrained optimization with interpretable feature streams, the proposed method improves inversion stability and robustness to spectral distortion without explicit DRM inversion or complex calibration. In simulations, the framework achieves an RMSE of 0.2111 for Z_{eff} estimation in the target low-Z range 6–13, while experimental validation on a CdZnTe-PCD yields an RMSE of 0.2457 with $R^2 = 0.9670$. Moreover, 92.86% of experimental samples exhibit absolute Z_{eff} estimation errors within ± 0.4, indicating a tighter error bound (approximately 20% smaller than the conventional ± 0.5 range) under realistic pulse pile-up and noise conditions.

2. Proposed physics-informed framework

Drawing upon the PINN architecture,[43,44] we propose a slope-sensitive PINN framework with multi-order differential feature fusion for distortion-robust material identification. The framework incorporates x-ray attenuation physics as embedded physical constraints and combines them with explicit feature engineering to achieve decoupled estimation of material parameters (Fig. 2). In PCD-based measurements, the observed spectra are jointly influenced by the polychromatic

x-ray source and the detector response function, causing excessive smoothing of raw attenuation signals and obscuring local nonlinear spectral characteristics related to the effective atomic number. To address this issue, we introduce a noise-robust explicit gradient module at the feature extraction front end.

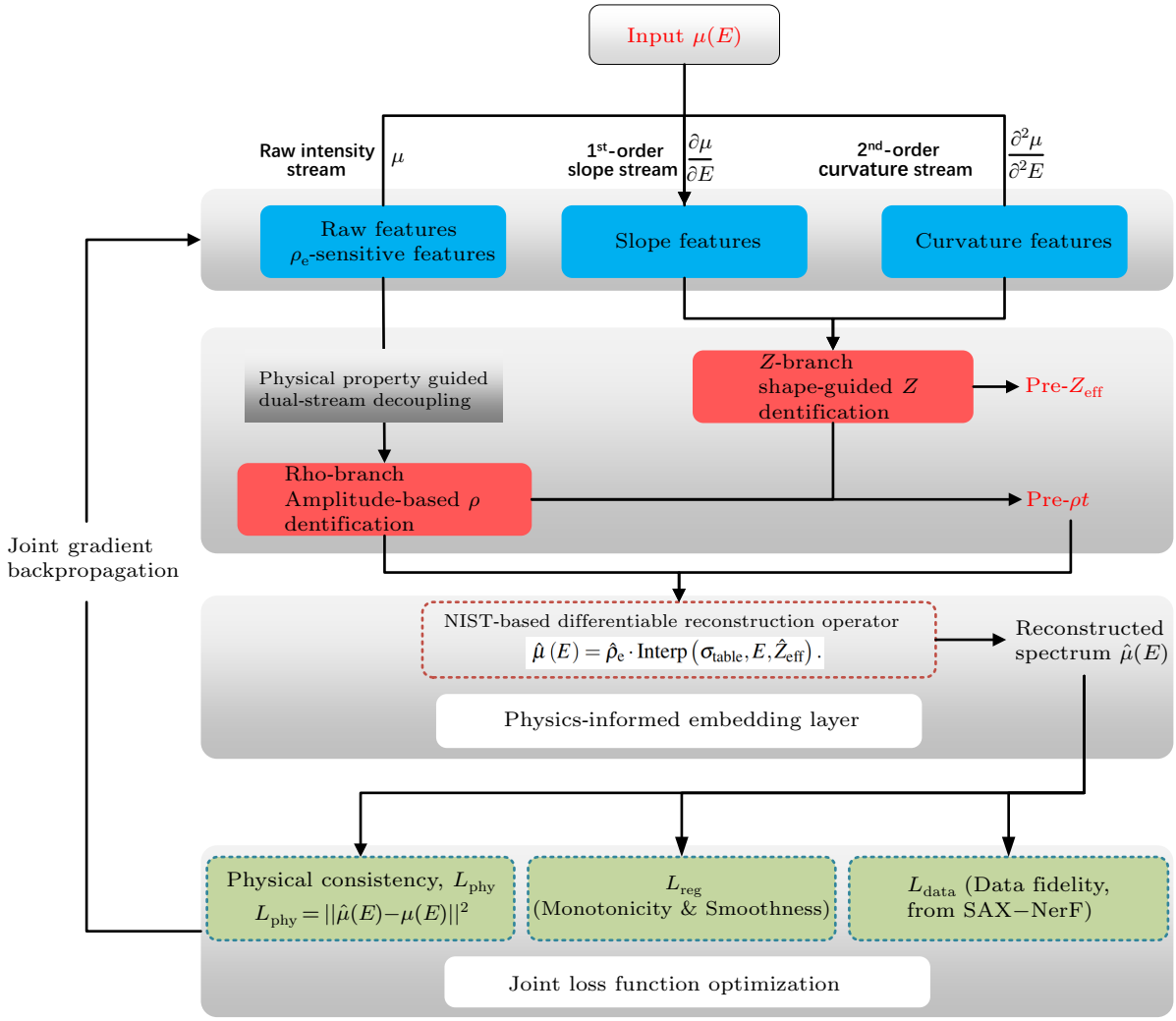


Fig. 2. Schematic illustration of the physical constraint mechanism in the proposed PINN framework.

By exploiting the high-pass filtering properties, the differential operator enhances Z-sensitive features latent within the spectral slope (1st order) and curvature (2nd order). This progression from 0th to 2nd order representations is physically consistent with high-order energy dependence of the photoelectric effect, thereby providing a more discriminative feature space for material identification. To improve robustness against photon statistical noise, the raw spectral vector is first processed by a learnable 1D smoothing convolution layer, which adaptively suppresses high-frequency noise while preserving the intrinsic spectral structure. The resulting features are then separated into three parallel streams: raw-intensity stream that preserves absolute attenuation amplitude (primarily related to areal density, ρt); first-order slope stream that captures energy-dependent attenuation trends; and second-order curvature stream that enhances spectral convexity associated with the Z-dependent nonlinear spectral behavior of the photoelectric effect. This design establishes the physical basis for subsequent decoupled inference of the effective atomic number and areal density. The present framework is mainly intended for low-Z materials in the range 6–20, whose attenuation spectra remain relatively smooth within 20 keV–80 keV.

To avoid the lack of interpretability in traditional feature concatenation, we design an asymmetric decoupling architecture. Atomic number branch (Z-branch): aggregates slope (1st order) and curvature (2nd order) features. Physically, Z dominates the "shape" and "curvature" of the attenuation curve via the photoelectric cross-section's energy dependence ($\sigma_{\text{pe}} \propto Z^3/E^3$). Consequently, this branch specifically aggregates the first-order slope and second-order curvature features, leveraging their translation invariance to amplitude variations to achieve robust estimation of Z. Electron density branch (ρ-Branch): Focuses on raw intensity features. The electron density (ρ_e) physically manifests as a linear multiplier, directly

determining the "amplitude" of the overall attenuation curve. Therefore, this branch prioritizes the raw intensity features. This strategy, predicated on the principle that spectral shape encodes Z while amplitude reflects ρ, effectively mitigates parameter coupling, thereby circumventing the ill-posed nature of the inverse problem.

We construct a differentiable forward operator based on the NIST physical database. The network predictions, $\left(\hat{Z}_{\text{eff}}, \hat{\rho}_{\text{e}}\right)$, are employed to reconstruct the theoretical attenuation spectrum, $\hat{\mu}\left(E\right)$, according to

$$\hat{\mu}\left(E\right) = \hat{\rho}_{\text{e}} \cdot \text{Interp}\left(\sigma_{\text{table}}, E, \hat{Z}_{\text{eff}}\right), \tag{2}$$

where Interp$(\cdot)$ denotes a bilinear interpolation function derived from the standard NIST cross-section database.

The loss function consists of three components: physical consistency loss, defined as the mean squared error (MSE) between the reconstructed spectrum $\hat{\mu}\left(E\right)$ and the network input $\mu\left(E\right)$; monotonicity and smoothness regularization, implemented as a derivative constraint,

$$L_{\text{smooth}} = \left\|\partial\hat{\mu}/\partial E\right\|^2, \tag{3}$$

which enforces the smooth and monotonic attenuation profiles characteristic of light materials within the studied energy range; and data fidelity term, which penalizes the discrepancy between the network outputs $\left(\hat{Z}_{\text{eff}}, \hat{\rho}_{\text{e}}\right)$ and the corresponding ground-truth labels $\left(Z_{\text{eff}}, \rho_{\text{e}}\right)$.

The proposed architecture comprises three sequential stages: data preprocessing and feature extraction, serial physics-based decoupling, and physics-constrained optimization. The network takes raw spectral data as input and first applies internal Z-score normalization using precomputed statistics to standardize the input distribution. A gradient-layer then performs finite difference calculations across energy points to extract gradient features. These features are processed by the Shape-CNN, which consists of three stacked slope-sensitive-blocks. Each block applies 1D convolutions with progressively expanding receptive fields to capture attenuation trends, followed by a MaxPool1d (2) layer to halve the sequence length. The output features are flattened and input into the Z_head (MLP) to predict the normalized effective atomic number.

To decouple the material parameters, a serial connection strategy is adopted. First, the predicted normalized Z is denormalized and passed to a differentiable physical operator (compute_mu) to calculate the theoretical unit-density attenuation coefficient. Second, the raw input spectrum is element-wise divided by this theoretical coefficient. This operation isolates the density-dependent amplitude by canceling out Z-related spectral shape components. Finally, the isolated amplitude is input into the rho_mlp to regress the normalized areal density. The network is optimized using a composite loss function that balances data fidelity with physical consistency. It comprises two terms: (1) data loss (loss_data), defined as the MSE between the predicted normalized parameters and their corresponding ground-truth labels; and (2) physical consistency loss (loss_pde), defined as the MSE between the measured raw spectrum and the spectrum reconstructed via the Beer–Lambert law. To ensure training stability, a step-wise curriculum learning strategy is applied: the weight of the physical loss is initialized to 0 during the warm-up period (e.g., 500 epochs) to prioritize data fitting, and is subsequently increased to a fixed constant (e.g., 0.2) to enforce physical constraints.

3. Results and discussion

We employed a dual-validation strategy comprising numerical simulations and physical experiments. Simulations probed the theoretical limits across a broad range of atomic numbers, while experiments validated robustness in real-world environments.

3.1. Simulation experiments

To construct a training dataset covering diverse spectral distortion characteristics, we performed forward physical simulations based on the NIST XCOM database and the Beer–Lambert law. The simulation encompasses a broad range of atomic numbers from carbon ($Z = 6$) to calcium ($Z = 20$), representing materials relevant to applications such as carbon-fiber composites and biological tissues. Using a Monte Carlo sampling strategy, we generated 490 theoretical samples with distinct combinations of effective atomic number (Z_{eff}) and mass thickness (ρt). Of these, 80% were allocated for network training and the remaining 20% for validation in the simulation experiments. Specifically, Z_{eff} was uniformly sampled within 6–20, while ρt was randomly sampled within 1–20 g/cm^2. To generate the corresponding network inputs, detector-response-induced spectral distortions were superimposed on the ideal attenuation spectra, including charge sharing, pulse pile-up, and Poisson noise.

The primary objective of the simulation validation phase is to assess the theoretical inversion capability of the PINN framework across a broad range of atomic numbers ($Z \in [6, 20]$). Since the simulated dataset preserves the nonlinear discontinuities inherent in the idealized physical model, this validation also provides a rigorous assessment of the network architecture's ability to enforce the embedded physical constraints.

Simulations evaluated the inversion capability across the range of $Z \in [6, 20]$. Overall, the model exhibits a high degree of consistency within this interval, with the predicted points tightly converging along the $y = x$ diagonal. These results demonstrate that the proposed method is well-suited for effective atomic number inversion within this specific range.

However, an examination of the error distribution reveals that as the atomic number increases beyond 13, discrepancies between the predicted and ground truth values become apparent, with the RMSE rising to 0.6729. This phenomenon is a direct consequence of the intrinsic physics of x-ray attenuation. Within the 20 keV–80 keV energy range, the photoelectric effect cross-section ($\sigma_{pe} \propto Z^3/E^3$) escalates rapidly as the atomic number Z increases. Consequently, higher-Z materials exhibit significantly steeper gradients and more pronounced non-linear curvature in their attenuation spectra. While the smoothness regularization term in the PINN framework effectively suppresses statistical noise, it may inadvertently dampen these intensified local non-linearities, leading to the observed underestimation of the attenuation amplitude.

To further examine the noise sensitivity of differential features such as the first-order slope and second-order curvature, especially under low-count or high-attenuation conditions where Poisson fluctuations become more pronounced, additional simulations were performed at different Poisson noise levels.

As the Poisson noise level increases from 1% to 20%, the Z_{eff} prediction error increases progressively. The model remains accurate and stable within the 1%–10% noise range. However, the error becomes noticeably larger at 15% noise, and significant outliers appear at 20% noise (RMSE = 1.0347, R^2 = 0.7381), indicating that the slope- and curvature-based Z_{eff} branch becomes unstable under high-noise conditions.

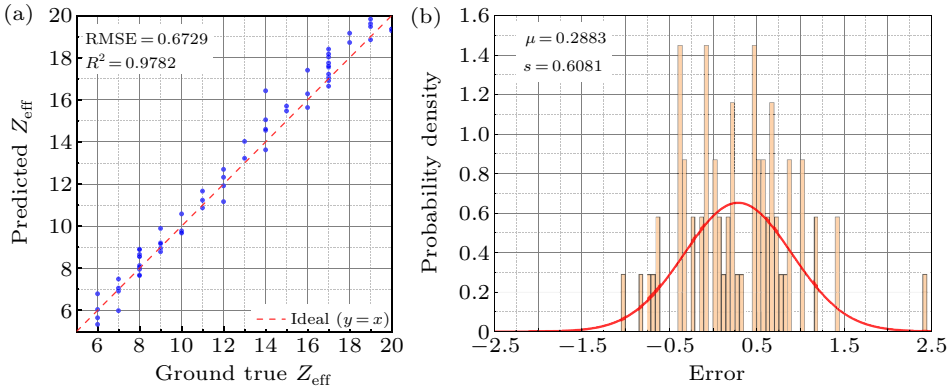


Fig. 3. Simulation results for Z_{eff} estimation under 1% Poisson noise. (a) Predicted versus ground-truth Z_{eff}. (b) Estimation error distribution of Z_{eff}.

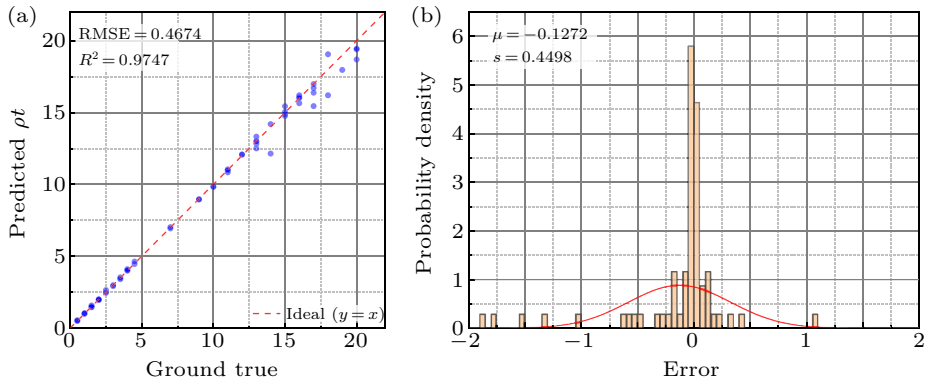


Fig. 4. Simulation results for ρt estimation under 1% Poisson noise. (a) Predicted versus ground-truth ρt. (b) Estimation error distribution of ρt.

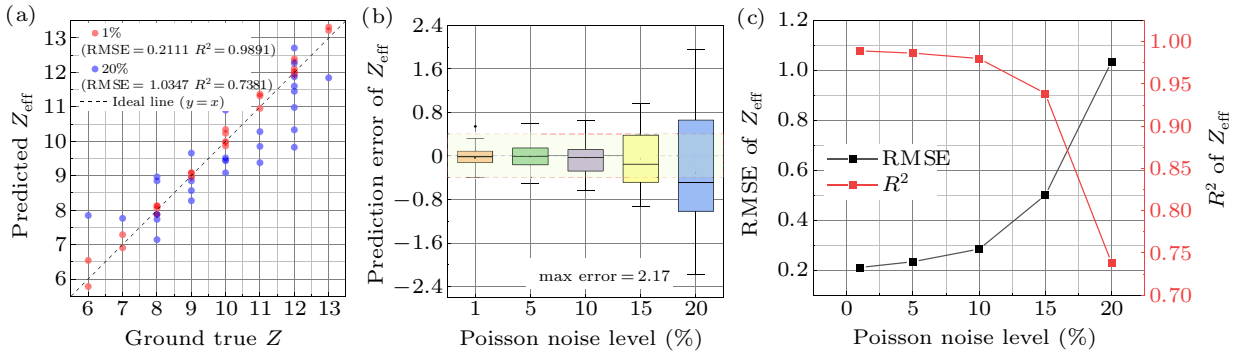


Fig. 5. Comparison of Z_{eff} prediction results under different Poisson noise levels. (a) Predicted versus ground-truth Z_{eff} under 1% and 20% Poisson noise. (b) Box plots of prediction errors under different noise levels. (c) RMSE and R^2 versus Poisson noise level.

4. Physical experiments

The experimental validation was conducted on an x-ray imaging platform equipped with a CdZnTe photon-counting detector. The x-ray source was operated at a tube voltage of 80 kV and a tube current of 0.3 mA, and spectral data were acquired across an energy range of 20 keV–80 keV (Fig. 6(a)). The experimental samples consisted of a continuously tunable PMMA/aluminum (PMMA/Al) mixture space and a separate set of independent pure materials (Fig. 6(b)). The conventional PMMA/Al combinations were used to construct the primary dataset, with the theoretical Z_{eff} for each mixture calculated via a weighted procedure based on standard NIST cross-sections. This dataset was partitioned into 80% for training and 20% for validation. By varying the thicknesses of the two slabs, phantom samples with different equivalent Z_{eff} and ρt were synthesized. An orthogonal grid of PMMA/Al combinations was constructed, in which the thicknesses of both PMMA and Al were varied over multiple levels from 3.7 mm to 40.7 mm.

To verify model generalization and prevent overfitting to the PMMA/Al training manifold, out-of-distribution physical samples were introduced during the testing phase. These independent targets included pure compounds (PTFE and standard PMMA) and single-element materials (carbon, $Z = 6$; Al, $Z = 13$). The measured samples exhibited an effective atomic number range of 6–13, which matches the physical characteristics of carbon-fiber composites, biological soft tissues, and common security-screening materials.

Before feature extraction, the raw measurements were preprocessed through repeated sampling, multi-pixel averaging, and denoising filters. These steps are necessary to suppress inherent Poisson noise and prevent its amplification by the differential layers. Figure 7 presents the quantitative results for Z_{eff} identification, offering a direct comparison between the experimental performance and the ideal simulation benchmark.

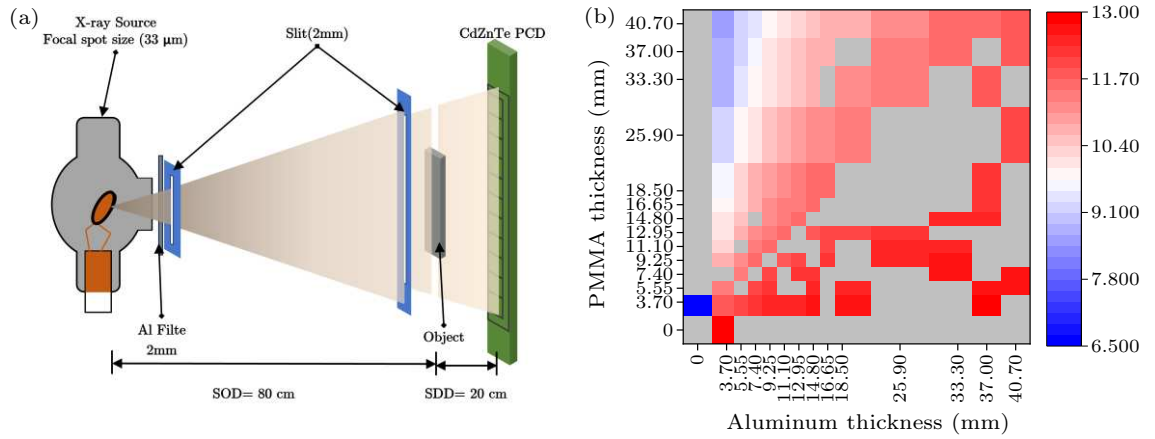


Fig. 6. Experimental setup and sample configuration. (a) X-ray imaging platform equipped with a CdZnTe photon-counting detector. (b) Experimental samples.

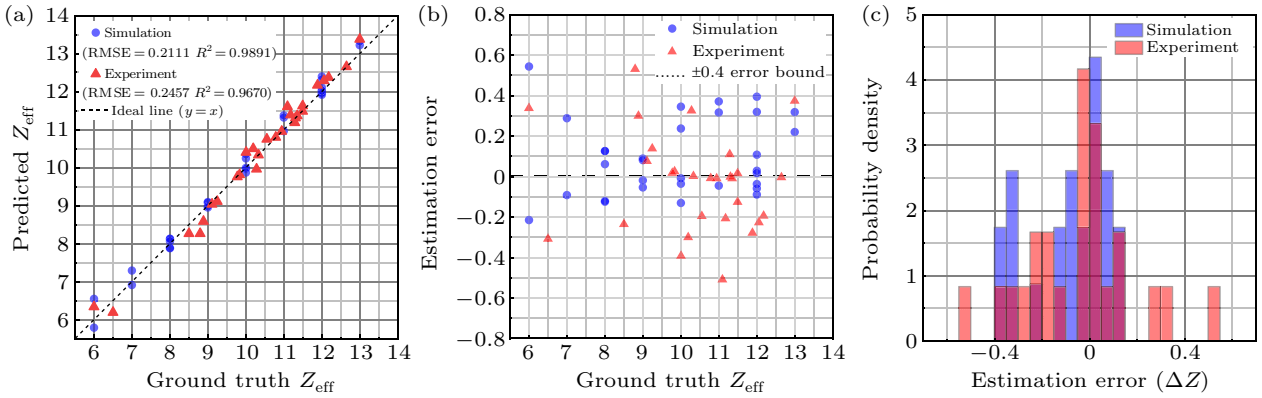


Fig. 7. Experimental results for Z_{eff} estimation. (a) Predicted versus ground-truth Z_{eff}. (b) Estimation error distribution of Z_{eff}. (c) Histogram of estimation errors.

As illustrated in Fig. 7(a), despite the inevitable presence of pulse pile-up effects and electronic noise in the hardware, the experimental predictions (red triangles) exhibit exceptional linearity, tightly converging along the ideal $y = x$ diagonal. Quantitative analysis yields a coefficient of determination (R^2) of 0.9670, which is comparable to the theoretical simulation benchmark of 0.9891. The RMSE for the experimental data is 0.2457. This high degree of consistency with the simulation result (RMSE = 0.2111) provides compelling evidence that the PINN framework effectively miti-

gates spectral distortions, successfully transferring theoretical high-precision performance to practical application scenarios.

Further analysis of the error distribution, shown in Figs. 7(b) and 7(c), underscores the reliability of the model. Although the experimental error distribution is slightly broader than that of the simulation, it displays no significant systematic bias. Notably, approximately 92.86% of the experimental samples exhibit an absolute estimation error within the safety bound of ± 0.4 (indicated by dashed lines in Fig. 7(b)). This result confirms that the method maintains high confidence in distinguishing materials with adjacent atomic numbers within the range of $Z \in [6, 13]$, thereby fully satisfying the precision requirements for industrial non-destructive testing.

In addition, comparison with the graded simulation results at different Poisson noise levels shows that the experimental performance (RMSE $= 0.2457$, $R^2 = 0.9670$) is close to that obtained under the 5%–10% Poisson noise condition. This suggests that, after repeated sampling, multi-pixel averaging, and denoising preprocessing, the measured data of the current experimental system have not yet reached the noise level at which the model becomes clearly unstable.

4.1. Analysis and discussion

The RMSE and the R^2 were adopted as the primary evaluation metrics. Table 1 summarizes the quantitative performance of the PINN framework across both simulation and experimental datasets.

Table 1. Quantitative comparison of simulation and experimental results.

Experiments	Z-range	RMSE	R^2
Simulation experiments (full range)	6–20	0.6729	0.9782
Simulation experiments (target range)	6–13	0.2111	0.9891
Physical experiments	6–13	0.2457	0.9670

Contrary to the divergence often seen in pure data-driven methods, our framework maintains high consistency between theoretical simulations and physical experiments. The simulation results established a theoretical high-precision benchmark (RMSE $= 0.2111$) within the atomic number range of 6–13. The experimental validation yielded a slightly higher RMSE of 0.2457. This marginal increment is physically consistent and anticipated, attributed to real-world hardware factors absent in the ideal simulation, such as electronic noise, dark current, and residual scattering effects. However, the fact that the experimental performance closely trails the ideal simulation benchmark (R^2: 0.9670 vs. 0.9891) demonstrates the regularization efficacy of the embedded physical constraints.

To rigorously validate the performance superiority of the proposed framework, we benchmarked our results against the conventional physical correction methods and the standard data-driven learning approaches. Conventional methods typically achieve an atomic number estimation accuracy of approximately ± 0.5.[25] As shown in Fig. 7(b), 92.86% of the test samples in the proposed method exhibit absolute estimation errors within ± 0.4, indicating a tighter error bound (by approximately 20%) under realistic experimental conditions. Standard data-driven approaches (e.g., A-table or Gaussian regression), while avoiding complex physical modeling, struggle to statistically decouple the non-linear relationship between Z and ρ due to the lack of rigid physical constraints. Experiments indicate that the proposed PINN method achieves higher prediction accuracy.

Table 2. Comparison of RMSE in Z_{eff} estimation against established methods.

Algorithm	PINN	A-table	Gaussian regression
RMSE	0.25	0.37	0.40

The PINN framework achieves both high consistency and high precision primarily due to the explicit gradient layer, which performs physically meaningful feature enhancement and decoupling. By explicitly extracting differential spectral features, this module improves the network's sensitivity to material-dependent spectral morphology while preserving robustness under spectral distortion. The underlying physical mechanism is discussed below.

Dominance of photoelectric interaction and first-order decoupling. The noise robustness is directly rooted in its response to the physics of the photoelectric effect. The core advantage of photon-counting detection lies in extracting energy information. Within the experimental energy range (20 keV–80 keV), x-ray attenuation is dominated by the photoelectric effect, the cross-section of which follows an approximate power law $\sigma_{\text{pe}} \propto Z^3/E^3$. The proposed first-order slope stream ($\partial\mu/\partial E$) mathematically extracts the local rate of spectral change, effectively isolating the "shape" features governed strictly by Z. This transformation separates the spectral morphology dominated by the photoelectric effect from the global amplitude fluctuations caused by electron density (ρ_{e}), endowing the network with translation invariance to object thickness and enabling robust Z_{eff} estimation.

Second-order curvature features and high-Z sensitivity. To further enhance material discrimination, especially for relatively high-Z materials, the 2nd-order curvature stream ($\partial^2\mu/\partial^2 E$) serves as a morphological feature detector. It enhances the sensitivity to the spectral convexity and non-linear transitions that define material fingerprints in the absence of K-edge signals within the measured window. As discussed by Hayashi *et al.*,[8] K-shell absorption edges provide element-specific signatures; however, the identification capability of the present framework does not rely solely on discrete K-edge discontinuities. Instead, it is primarily derived from high-order

spectral curvature features induced by the photoelectric effect. In this sense, the second-order derivative acts analogously to a discrete Laplacian operator, enhancing sensitivity to local spectral curvature and nonlinear transitions.

While the curvature branch improves sensitivity to the Z-dependent nonlinear attenuation profile and enhances material separability by amplifying spectral convexity, the increased error in the high-Z region should not be attributed to the smoothness term alone. As the atomic number increases, the local spectral nonlinearity becomes stronger, and the extraction of curvature features places higher demands on the stability of finite-difference estimation. The present differential-feature extraction and smoothness prior were mainly developed for the relatively smooth attenuation spectra of low-Z materials, and their suitability may decrease as sharper local spectral features emerge. In addition, a more fundamental limitation comes from photon starvation: for the higher-Z materials within the 6–20 range, the stronger attenuation of low-energy photons reduces the effective transmitted counts and the amount of usable discriminative information, thereby increasing the instability of derivative-based features. The degradation observed in the high-Z region is therefore more reasonably understood as the combined effect of reduced suitability of the smooth differential prior and information loss caused by photon starvation.

At the same time, we also note an increased estimation error near the lower boundary ($Z = 6$). Rather than a simple dataset boundary effect or model overfitting, this is driven by fundamental x-ray physics. For ultra-low-Z elements like carbon in the 20 keV–80 keV range, attenuation is dominated by Compton scattering instead of the photoelectric effect. Since the Compton cross-section is weakly dependent on photon energy, the resulting attenuation spectra are remarkably flat. This physical reality inherently diminishes the slope and curvature features required by the network for accurate Z discrimination.

5. Conclusion

This study proposes a PINN framework to address spectral distortion in PCDs. By embedding an explicit differential layer within a physics-guided decoupled architecture, the method effectively overcomes the ill-posedness of traditional matrix inversion. Experimental validation on a CdZnTe-PCD demonstrated exceptional robustness, achieving an RMSE of 0.2457 ($R^2 = 0.9670$), which closely aligns with the theoretical simulation benchmark (RMSE = 0.2111). This performance enhancement is attributed to the network extracting high-order spectral curvature features induced by the photoelectric effect. Future work will address the limitation of time-consuming full-spectrum scanning by exploring discrete multi-energy bin strategies. Leveraging the established physics-constrained model, we aim to optimize the selection of energy bins most sensitive to high-order spectral curvature, thereby facilitating real-time industrial applications.

Acknowledgment

Project supported by the Natural Science Basic Research Program — General Program (Grant No. 2025JC-YBMS-712).

References

[1] Wen X, Chen S, Song K, Yu H, Li X and Zhong L 2025 *Comput. Mater. Contin.* **85** 4173
[2] Morigi M P and Albertin F 2022 *J. Imaging* **8** 119
[3] Schwartz F R, Sodickson A D, Pickhardt P J, Sahani D V, Lev M H and Gupta R 2025 *Radiology* **314** e240662
[4] Johns H E and Cunningham J R 1983 *The Physics of Radiology*, 4th edn. (Springfield: Charles C Thomas) p. 134
[5] Alvarez R E and Macovski A 1976 *Phys. Med. Biol.* **21** 733
[6] Taguchi K and Iwanczyk J S 2013 *Med. Phys.* **40** 100901
[7] Kreisler B 2022 *Eur. J. Radiol.* **149** 110229
[8] Hayashi H, Kimoto N, Asahara T, Asakawa T, Lee C and Katsumata A 2021 *Photon Counting Detectors for x-ray Imaging: Physics and Applications* (Cham: Springer) p. 59
[9] Schlomka J P, Roessl E, Dorscheid R, Dill S, Martens G, Istel T, Bäumer C, Herrmann C, Bonn R, Fink C, Nikisch E, Mattson J, Carmi R and Proksa R 2008 *Phys. Med. Biol.* **53** 4031
[10] Cammin J, Xu J, Barber W C, Iwanczyk J S, Hartsough N E and Taguchi K 2014 *Med. Phys.* **41** 041905
[11] Ponchut C 2008 *Nucl. Instrum. Methods Phys. Res. A* **591** 311
[12] Hong W, Wen X L, Wei L, Zhu B, Wu Y C, Dong K G, Jiao C Y, Wu B and He Y L 2017 *Chin. Phys. B* **26** 025204
[13] Guo R R, Xu Y D, Zha G Q, Wang T and Jie W Q 2018 *Chin. Phys. B* **27** 127202
[14] Nan R H, Wang P F, Jian Z Y and Li X J 2017 *Acta Phys. Sin.* **66** 206101 (in Chinese)
[15] Yu H, Zhang M M, Du Y Y, Xi S Z, Zha G Q and Jie W Q 2021 *J. Synth. Cryst.* **50** 1883
[16] Zhu W F, Wu J J, Tang X Q, Zhao R, Lu P Z, Qu B B, Li M Y and Qin F 2023 *Nucl. Tech.* **46** 050402
[17] Cao M, Deng J, He W, Zhou Y, Xie R, Jiang Y and Wang L 2023 *Appl. Phys. A* **129** 595
[18] Zakharchenko A A, Rybka A V, Davydov L N, Vierovkin A A, Kutny V E and Khazhmuradov M A 2014 *East Eur. J. Phys.* **1** 68
[19] Nag R, Chaudhuri S K, Kleppinger J W, Karadavut O and Mandal K C 2021 *J. Mater. Sci. Mater. Electron.* **32** 26740
[20] Roy U N, Camarda G S, Cui Y, Yang G and James R B 2021 *Sci. Rep.* **11** 10338
[21] Hu K, Li F, Chen L, Liang F T and Jin G 2015 *Chin. Phys. Lett.* **32** 030701
[22] Kimoto N, Hayashi H, Nishigami R, Kobayashi D, Maeda T and Katsumata A 2024 *Emerging Radiation Detection* (Cham: Springer) p. 69
[23] Kimoto N, Nishigami R, Kobayashi D, Maeda T, Asahara T, Goto S, Kanazawa Y, Katsumata A, Yamamoto S and Hayashi H 2026 *Radiat. Phys. Chem.* **239** 113237
[24] Shikhaliev P M 2012 *Phys. Med. Biol.* **57** 1595
[25] Kimoto N, Hayashi H, Asakawa T, Lee C, Asahara T, Maeda T, Goto S, Kanazawa Y, Katsumata A, Yamamoto S and Okada M 2021 *Appl. Radiat. Isot.* **170** 109617
[26] Murata K and Ogawa K 2021 *Sci. Symp. Med. Imaging Conf.* (Piscataway) p. 1217
[27] Sasaki T, Kuno H, Nomura K, Muramatsu Y, Aokage K, Samejima J, Taki T, Goto E, Wakabayashi M, Furuya H, Taguchi H and Kobayashi T 2025 *Jpn. J. Radiol.* **43** 1132
[28] Lantz M and Ongie G 2023 *Proc. IEEE 20th Int. Symp. Biomed. Imaging* (Cartagena) p. 1
[29] Darui L, Jordan M M and Willie J P 2025 *ACS Photonics* **12** 6071
[30] Chaudhuri S K, Kleppinger J W, Karadavut O, Nag R, Panta R, Agostinelli F, Sheth A, Roy U N, James R B and Mandal K C 2022 *J. Mater. Sci. Mater. Electron.* **33** 1452

[31] Nadkarni R, Allphin A, Clark D P and Badea C T 2022 *Phys. Med. Biol.* **67** 155003
[32] Eguizabal A, Öktem O and Persson M U 2022 arXiv:2208.03360 [physics.med-ph]
[33] Weiss M, Brierley N, von Schmid M and Meisen T 2024 *NDT* **2** 1
[34] Raissi M, Perdikaris P and Karniadakis G E 2019 *J. Comput. Phys.* **378** 686
[35] Chen Y, Lu L, Karniadakis G E and Dal Negro L 2020 *Opt. Express* **28** 11618
[36] Baldan M, Di Barba P and Lowther D A 2022 *Proc. IEEE 20th Biennial Conf. Electromagn. Field Comput.* (Denver) p. 1
[37] Zhang R, Li F and Liu J 2026 *Chin. Phys. B* **35** 030201
[38] Guo J, Wang H, Gu S and Hou C 2024 *Chin. Phys. B* **33** 050701
[39] Li W K, Zhao Z and Zhang Y T 2025 *Acta Phys. Sin.* **74** 235207 (in Chinese)
[40] Liu X M, Zhang Z Y and Liu W J 2023 *Chin. Phys. Lett.* **40** 070501
[41] Tian S F, Li B and Zhang Z 2024 *Chin. Phys. Lett.* **41** 030201
[42] Adler J and Öktem O 2018 *IEEE Trans. Med. Imaging* **37** 1322
[43] Toscano J D, Oommen V, Varghese A J, Zou Z, Ahmadi Daryakenari N, Wu C and Karniadakis G E 2025 *Mach. Learn. Comput. Sci. Eng.* **1** 15
[44] Yang S, Kim H, Hong Y, Yee K, Maulik R and Kang N 2024 *Comput. Methods Appl. Mech. Eng.* **428** 117075